Probing the irregular lattice strain-induced electronic structure variations on late transition metals for boosting the electrocatalyst activity

*Tong Wu, Mingzi Sun and Bolong Huang**

T. W., M. S. and Prof. B. H.
Department of Applied Biology and Chemical Technology, The Hong Kong Polytechnic University, Hung Hom, Kowloon, Hong Kong SAR, China
E-mail: bhuang@polyu.edu.hk

Keywords: strain effect, d-band-center, density functional theory, late transition metals, crystal facet

Owing to the simplicity in practice and continuous fine-tuning ability towards the binding strengths of adsorbates, the strain effect has been intensively explored, especially focused on the modulation of catalytic activity in transition metal (TM) based electrocatalysts. Recently, more and more abnormal cases have been found that cannot be explained by the conventional simplified models. In this work, the strain effects in five late TMs, Fe, Co, Ni, Pd, and Pt have been studied in-depth regarding the facet engineering, the surface atom density, and the d-band center. Interestingly, the irregular response of Fe lattice to the applied strain has been identified, indicating the untapped potential of achieving the phase change by precise strain modulation. For the complicated high-index facets, the surface atom density has become the pivotal factor in determining the surface stability and electroactivity, which identifies the potential of high entropy alloys (HEA) in electrocatalysis. Our work has supplied insightful understanding and significant references for future research in subtle modulation of electroactivity based on the precise facet engineering in the more complex facets and morphologies.

1. Introduction

The development of renewable energy industries is eagerly demanding novel high-efficiency and low-cost catalysts to achieve the practical large-scale application of new energy devices.[1–4] Transition metals have been found to be highly active towards the catalysis of several important electrochemical reactions related to energy conversions, such as oxygen reduction

reaction (ORR) and hydrogen evolution reaction (HER).[4–8] However, the electronic properties of transition metals require further optimization to reach a satisfying balance between catalytic efficiency and cost.[9] Nanoengineering, atom-doping, defect-engineering and alloying of transition metals have been studied extensively in an attempt to improve their reactivity. Still, it is challenging for these methods to adjust the activity continuously since the present introduced additional factors (e.g., ligand effects and changes in composition from doping or alloying) interrupt the precise interpretation of the electronic structure of the transition metals. A systematic method for continuous and direct adjustment of electronic structures is therefore in high demand. Strain tuning thereby becomes a promising candidate and has been extensively studied both theoretically and experimentally for the past decade. [5,8,10–30]

The applied strain on transition metal surface alters the distance between surface atoms and layers and subsequently modifies the electronic structures of the surface. Nørskov *et al*. [9,31] have concluded that for late-transition metals with over half-filled d-band, the tensile strain strengthens the bonding interaction with adsorbates while the compressive strain weakens the adsorption strength. Meanwhile, for early-transition metals with less filled d-band, the effect of tensile strain and compressive strain is the opposite. This theoretical model of how strain affects the d-band of transition metal surfaces has successfully instructed several attempts in the optimization of the transition metal catalysts.[24,32] In recent years, some exceptional cases have been noticed, which do not follow the prediction of the conventional theoretical model. For example, Gro *et al.* reported that the tensile strain on Cu (110) increased the hydrogen adsorption strength while the tensile strain on Cu (100) weakened the adsorption.[21] A DFT study of Liu *et al.* reported that the CO oxidation reaction barrier could be lowered by the tensile strain with the CO adsorption strength becoming weaker. In addition, for the hydrogen dissociation reaction on Pd and Cu deposited on a Ru (0001) substrate, theoretical calculation revealed that both the expanded Cu (111) and the compressed Pd (111) on Ru substrate are able

to activate the reaction.[14] Recently, Guo *et al.* group reported that the tensile strain on Pt (110) facet of the PtPb/Pt nanoplates facilitates the ORR activity by weakening the Pt-O bond strength to the optimized level.[10] More importantly, understanding the strain effect is also of pivotal significance to the synthesis and utilization of high-index facets of lattice in enhancing the catalyst performance, which displays more active sites. However, from our knowledge, strain effect on high-index facets has not been systematically studied and reported before, neither by experimental techniques nor theoretical calculations.

Herein, we conducted theoretical calculations by density functional theory (DFT) to systematically investigate the strain effect on five late-transition metals, Fe, Co, Ni, Pd, and Pt regarding the lattice response, electronic structures, and electroactivity. Irregular responses to the strain that are deviated from the prediction of the traditional interpretation are observed, [9,24,26,27] especially from (110) and (100) facets. While Ni and Co are generally subject to the conventional prediction of strain effect, Fe, Pd, and Pt both present unpredicted response to strain to various extent. The subsequent analysis in d-band and geometric changes revealed a correlation between the variation of interlayer distance of the surface and sub-surface layer with the changes of d-band properties. Meanwhile, the intriguing impact of strain onto the up-spin and down-spin portion of d-band is noted. Similar to the low-index facets, the stability, activity, and tendency of phase-transition of high-index facets have been systematically screened as well. The surface atom density of the kink atom has been identified as a potential universal descriptor of electroactivity, especially for the facets with high miller indexes. This finding largely facilitates the understanding of the unique properties of complex metal materials such as the high-entropy alloys (HEAs) from the general perspectives of surface atom density and surface energies. The screening of strain effect on high-index facets undoubtedly depicts a broader vision for the material science on more sophisticated nanomaterials.

2. Results and discussions

2.1 Non-monotonic trends of d-band center vs strain.

Under the conservative electron-filling constraints, the tensile strain narrows and sharpens the electronic band since the overlap between orbitals is weakened by the increased distance between atoms. In this sense, the shape modification of the band, especially the d-band in a transition metal, also affects the electronic property of the strained material.[18] The d-band center model proposed by Nørskov *et al.* characterizes the d-band reactivity by the first moment of the d-band density of states (DOS), which is the well-known d-band center.[31] The traditional understanding of the strain effect is the tensile strain upshifts the d-band center with stronger adsorption while the compressive strain weakens the adsorption by downshifting the d-band center. A recent study on early transition metal reveals that the above trend is only applicable to late-transition metals with their d-bands more than half-filled.[20] For the early-transition metals with d-bands less than half-filled, strain shows a converse trend. To verify the trend of the established models, we present the study of five late transition metals Pt, Pd, Fe, Co, and Ni with three low index surfaces (111), (110) and (100). Conventionally, it is expected that the d-band center position shifts linearly upward when the strain nature varies from compressive to tensile. The d-band center levels were obtained accordingly (**Eq S1**), and the variation trends of the metal surfaces under the -4% to 8% strain levels are summarized and the d-band center levels of each surface are shown in the scale bars. (**Figure 1a-c, Table S1**). With the color changing from blue to red, the value it represents increases monotonically. Hence, the relative variation trend of data from each element and facet under the given series of strain is displayed. The ideal prediction of the d-band center trend is also plotted in **Figure 1d** for comparison, which shows a linear evolution as the traditional prediction on strain effect.

Notably, only the (111) facet dataset follows the conventional prediction, whereas the (100) and (110) heatmaps of all elements reveal the non-linear trend (**Figure 1a-c)**. Co and Ni present mostly linear trends as the classic interpretation, where two facets display the linear trends. On the other hand, Pt only follows the classic interpretation in (111) facet, thus it is classified into the second category where the classic interpretation is limited to one facet only. Most importantly, none of the Fe and Pd facets follow the classic interpretation, where Fe displays the volcano trends and Pd exhibits the zig-zag trends. Hence, they are classified into the third category, as the classic interpretation fails completely in predicting their d-band center variations. From the perspective of facet, it is easily concluded that the classic interpretation only valid generally on (111) facets. Such deviation from the linear prediction of the d-band center against applied strain causes the difficulty in the design of strain-tuned transition metal catalysts and raises unexpected modulation results in experiments. Therefore, the classic interpretation of the effect of strain has been an oversimplified interpretation of the synergy effect among the geometric factors and electronic factors. Pd demonstrates the dramatically irregular variation of d-band under the applied strain. Thus, we proposed that the geometric changes upon lattice strain are much more complicated than expected, which substantially contributes to the local electronic structure. With this concept, we moved on to analyze the structural changes in the simulation models after the geometry optimization calculations in DFT.

2.2 The d-band modulation against the Interlayer bondlengths variation

The conventional interpretation of the strain effect vaguely correlates the variation in geometry with the bonding interaction between atoms. It is well-accepted that except the s-orbitals, the bondings between atoms require matches in both direction and symmetry. The strain induced structural changes inevitably imposes an impact on the bonding condition to various extent, depending on the consistency between the direction of structural deformations and orbital direction. Our theoretical calculations of the d-band center variation trends already highlight

that the applied strain invokes a different level of changes in the d-band. To illustrate the difference more clearly, the boxplot of d-band center values of all the facets and elements is given in **Figure 2**. The interquartile ranges (IQR), which are the sizes of the boxes and indicate the spread of the dataset, obviously differ significantly among facets and elements (**Figure 2a**). It is interpreted as the modulation capability of lattice strain towards the d-band of the surface atom. Hence, the strain modulation of the electronic structure has been proved that it is not universally effective for transition metals and specific facets. For instance, Pt and Ni, the strain modulates the d-band center effectively for Pt (111), Ni (111) and Ni (110) surfaces while both Pt (100) and Ni (100) are just slightly affected, especially the Pt (100).

In order to probe into the correlation between geometric change and electronic structure change, the bondlengths for the central atoms in the surface layers of all geometry-optimized models are analyzed. The bonds of central atoms are preliminarily categorized into two types: surface bonds and interlayer bonds, which are the bonds between the central atom and neighboring atoms in the surface layer, and the bonds between the central atom and neighboring atoms in the subsurface layer, respectively. The average bondlengths of surface bonds and interlayer bonds are plotted into the boxplots in **Figure 2b-2c**, respectively. Comparing these two figures against the d-band center boxplot, the interlayer bonds present a higher similarity in IQR and median values, while the surface bondlength shows the low correlation in the two stats. Except for Pd, the larger IQR of interlayer bondlengths corresponds to a larger IQR of d-band centers and vice versa. When comparing the median values within the data of the same elements, high similarity also presents between the d-band centers and interlayer bondlengths. The Pt (100) stands out as it features the extremely narrow IQR in both d-band centers, surface bondlengths and interlayer bondlengths. These results suggest that the Pt (100) facet lattice barely yields to the applied strain, and the negligible variation in structure subsequently leads to the negligible variation in electronic structure.

2.3 Element Dependent Strain Investigation

The above analysis of bondlengths variation upon lattice strain unravels that the actual response of strain of the surface layer is directional. To better demonstrate the detailed geometric change of the surface layer under applied strain, we derived the “local atomic strain" parameter from the definition of lattice strain shown in the supporting information. The calculated atomic strain reveals that for bonds between the surface atoms, the extent of bondlength variation is highly overlapped with the applied strain level. In contrast, the interlayer bondlengths demonstrate distinct trends compared to those of surface bondlengths and lattice strain. In other words, the interlayer interaction under the effect of strain is facet- and element-wise dependent. [15,33,34] In particular, for certain facets, the interlayer bondlengths are consistently compressed or stretched regardless of the nature of applied lattice strain. Therefore, the conventional model that simply assumes tensile strain increases atomic spacing and the compressive strain does the opposite is not applicable for these cases and further misleads the prediction. Detailed Discussion has been supplied in **Supporting Information Figure S1-S4**. Since a detailed examination of the surface geometries and potential active sites is still a great challenge to the experimental techniques, theoretical studies are able to undertake the important role to supply essential microscopic information.

2.4 The d-band properties and interlayer distance

Besides the investigation of d-band center values, we also conducted visual inspections on the plotted d-bands extracted from the central atom of each analyzed model. Since the d-band center is a measure of the average energy level of the d-band, it actually provides limited information about the d-band properties, especially in the distribution and shape. The importance of the shape of DOS has been well recognized in previous researches. [35,36] According to the conventional interpretation of the effect of strain, the d-band shape is narrowed or widened

depending on the compressive or tensile nature of strain. For the DOS of d-bands in most elements, the conventional prediction is valid while in several cases mutations in d-band are also observed. The most obvious d-band shape mutations are observed in Fe (110) and Fe (100) (**Figure 3a-3b**). The d-band shape mutation is defined as the obvious change in the number of peaks in DOS and the overall shape of d-band. For Fe (110), the d-band shapes of 0%, 2%, and 7% strain levels are significantly changed, while the other d-bands DOS with similar strain levels are similar in shape. For Fe (100), the d-bands under -2% and -1% strain are different from the others, while the d-band at 6% strain presents a change in the portion above the Fermi level. The schematic illustration of the relevant interlayer bonds are presented in **Figure 3c-3d**, and the bondlengths results are shown in **Figure 3e-3f** and **Table S2**-**S3**. Through the detailed bondlength data, a correlation between the d-band mutation and the interlayer bondlengths is identified. It is observed that for those surfaces with similar strain levels and similar bondlengths, their d-band shapes are also similar with minor differences in width and height. For the surfaces with mutated d-band, their interlayer bondlengths also experience erupted changes. The surface bondlength generally varies linearly and monotonically as the strain changes from compressive range to tensile age. Combining with the boxplot analysis, the geometric change in the direction perpendicular to biaxial applied strain plays the dominant role in affecting the electronic structure properties for the late transition metals.

2.5 Spin-dependent d-band analysis.

In the discussion above, we observed the irregular zig-zag and volcano like d-band center variation trend with strain. Our DFT calculations have taken spin-polarization into consideration to interpret the intriguing trends. The d-band of the surface is divided into the alpha- and beta- portion, which resembles the spin-up and spin-down state of the d-band. For the metals with intrinsic spin, their alpha and beta DOS generally shift away from each other in energy with a similar shape. Although the difference between two d-band portions is observed

visually, a quantitative analysis approach of the spin-specific DOS is the prerequisite of a systematic study. We propose a mathematical-based approach to quantitatively compare and analyze the two spin DOS of each surface model. DOS is viewed as a probability distribution with a large data set since the number of data points in DOS usually exceeds 1000. For this kind of distribution, the Two-sample Kolmogorov-Smirnov (KS) Test is introduced to determine the similarity of the two spin DOS portion statistically.[37,38] The testing of the method confirmed its validity for the distinguish of the subtle DOS difference, which has been discussed in the supporting information (**Figure S5, Table S4-S6**).

The previous discussion of d-band center variation with applied strain reveals that the Pd and Fe demonstrate an unexpected "volcano" trend under the applied strain. The highest d-band center positions for Pd and Fe appear at moderate tensile strain range while increasing compressive strain or tensile strain both lead to downshifts of the d-band average energy. We applied the spin-specific analysis method to reveal more details about the electronic structure change in response to the lattice strain. Since the (110) facets were reported to have the most irregular d–band center trends in number (**Table S1**), the (110) metal surfaces were analyzed first in an attempt to find out the underlying mechanisms. The d-band center shifts relative to its position at zero strain for each metal (110) surface are plotted in **Figure 4**. Pt (110) displays a little range of variation with a zig-zag like trend (**Figure 4a**), where an intriguing opposite effect to the two spin portions of Pt d-band appears at the compress strain of 1%. The d-band center for the alpha-spin portion is largely pushed up whereas that of the beta-spin portion is pushed down. The competitive energy change of both portions results in the small variation in the total d-band center positions. The alpha- and beta-spin d-band center shifts of Pd (110) resemble that of Pt (110) at the compressive range. The strain shifts the average energy level of the two spin-portions in opposite directions, and hence the general d-band center shifting trend becomes hard to predict by the nature of strain (**Figure 4b**). Ni (110) surface demonstrates the

only trend that is consistent with the conventional theory prediction, where the alpha- and beta-spin of Ni (110) d-band changes synchronically (**Figure 4c**) Although an exceptional rise of energy in a compressive strain of 2% is observed, Ni (110) still generally follows the prediction that compressive strain downshifts the d-band energy while tensile strain upshifts the energy. For Fe (110), the peak of the volcano is located at zero strain level, from where the beta-spin of Fe (110) is consistently shifted downwards to lower energy level when the strain increases in either compression or tensile directions (**Figure 4d**). Meanwhile, the alpha portion energy shows a gradually decreasing trend when the strain turns from compressive to tensile, which is more like the one predicted for early-transition metal by the previous theories. This confirms that applying a compressive strain or tensile strain cannot push the Fe (110) d-band center to a higher level, but only to shift it downwards. For another "volcano", the d-band shifts of Fe (111) facets behave similarly to Fe (110). However, the beta portion follows the prediction of the d-band model, where the energy goes up when the strain becomes tensile and goes down when the strain becomes compressive (**Figure 4e**). The alpha portion shows the opposite trend. The competing changing trend of two portions results in the volcano plot for the d-band center when averaging the two spin portions. The Pd (111) also resembles those of Pd (110) (**Figure 4f**). The difference is that the two spin portions of Pd (111) d-band eventually shift towards higher energy at a strain level above 6%. In summary, the spin-dependent d-band analysis demonstrated that the irregular responses to strain in d-band centers are highly correlated with the distinct impact on the two spin-portion of d-bands brought by the applied strain.

2.6 Strain effect to high-index facets

Metal nanocrystals with high index facets typically possess a high density of steps, ledges, and kinks on the surface, which are the essential active sites for facilitating the electrocatalysis process and endow them the potential for different reactions. However, due to the intrinsic instability of the high-index facets induced by strain and higher surface energies, the

stabilization and preservation of these facets are very challenging during the nanocrystal synthesis. More importantly, most investigation of strain effect excludes the high-index facets, which still requires the in-depth exploration and analysis to further assist the experimental synthesis of the electrocatalyst. Hence, we further conducted theoretical calculations on the high-index facets of late transition metals regarding the stability, the corresponding geometric and electronic properties changes with applied strain.

The stability of the facet is evaluated by the facet formation energy and surface energy. As **Figure 5a** shows, the facet formation energies reflect the internal property difference between elements. Pd facets have the highest facet energies while the Pt facets have the lowest. The sizes of data points are determined by $m = \sqrt{h^2 + k^2 + l^2}$ from miller index to indicate the scale of the index. The surface atom density is calculated by dividing the number of surface layer atoms by the surface area of the lattice model. Hence, the larger the miller index, the smaller the surface atom density. The electronic properties are represented by the d-band center values of the atom on the step or kink on the facet surface, which are denoted as “surface" and “single" respectively. **Figure 5b-c** plotted the d-band center values against the facet formation energies. The facets of five elements clustered onto five islands on the figure, with subtle discrepancies between the facets within the same elements. The trend for the energies and d-band centers of high-index facets is therefore obscured.

Consequently, the correlation between surface energy and surface atom density confirms the surface energies for high-index facets eventually approaches zero as the corresponding surface atom densities approach zero for all elements. With the combination of surface energy and surface atom density, the facet stability trend is distinguished within the same element and converges to a unified end for all elements, which also conveys the identity of the element implicitly (**Figure 5d**). Regarding the stabilities of facets, surface energy is an essential

parameter to reveal the internal relation between the surface atom density and facet stability. Notably, the surface energy distinguishes the stability difference of the various facets of each element, as the clusters on the facet energy vs. d-center figure are untangled (**Figure 5e-f**). The figure clearly demonstrates that facets with relatively high stability and preferable d-center position. Pt has facets with remarkable stability and deep position of d-band center. Fe also has several relatively stable facets with shallow d-band centers. Co and Ni facets present similar levels of stability and d-band center position. Pd facets are the most unstable ones with similar d-band center positions to those of Pt facets. For the dependence of surface energies on the miller index, we notice the exponential trend for all the elements, indicating the strong correlation between the surface stability and the miller index (**Figure 5g**). Moreover, the surface atom density as the descriptor is also able to reveal the intrinsic electronic structure difference of each element, supporting its promising application in other materials (**Figure 5h-5i**). Therefore, this surface atom density has the potential to extend to other facets or even amorphous surfaces to become a universal descriptor of the surface stability and activity, which overcomes the complicity induced by the specific morphology and configuration differences. In this way, the scaling relationship, which is the long-lasting limitation of a heterogeneous catalyst, is substantially overcome by constructing corresponding active sites for target intermediates.

To further unravel the underlying correlation between the facet and surface energies and electroactivity, we introduce the structural entropy S to derive the correlation, which has been represented by the follows.

$$S = k_B \ln W \quad (1)$$

In this equation, k_B is the Boltzmann constant and W represents the local atomic possibility, which consists of ion W_{ion} and electron W_e arrangement possibility for the single metal

electrocatalyst. By connecting with the thermodynamic expressions with temperature T and initial facet energy E_0, we derive the following correlation.

$$E = E_0 \ln(m) = -TS = -k_B T ln(W_e \times W_{ion}) \quad (2)$$

Then we deduce the following relationship as Equation (3)-(4) by the introduction of m from miller index.

$$\ln(W_e \times W_{ion}) = \left(-\frac{E_0}{k_B T}\right) \ln(m) \quad (3)$$

$$W = \exp\left[m^{\left(-\frac{E_0}{k_B T}\right)}\right] \quad (4)$$

Such a correlation indicates that the electroactivity of high index facet cannot keep increasing, which reaches the limits after certain index facets. With such a surface, E_0 is approaching 0, representing that $W_e \times W_{ion} \approx 1$ indicating the limits of electroactivity enhancements. Thus, this confirms the existence of the "lock-in effect" during the electroactivity modulation by the high-index surfaces. The different exponential correlation of different elements indicates the intrinsic electroactivity and modulation capability of each single transition metals.

For the alloys or even complicated HEA materials, we further derive our above equations by introducing the S_{mix} as the mixing entropy to the total structural entropy S. Then we have the following derivations, where S_e and S_{atom} are the electron entropy and atomic entropy, respectively.

$$E = E_0 \ln(m) = -TS = -TS_e - TS_{atom} - TS_{mix} \quad (5)$$

$$S_{mix} = -\frac{1}{T}[E_0 \ln(m) + TS_e + TS_{atom}] \quad (6)$$

Thus, we construct a comparison of entropy between amorphous and ordered material systems. For an ordered material system with fixed components, $TS_e + TS_{atom}$ should be constants. For the amorphous HEA structures with high entropy S_{mix}, only decreasing the $E_0 \ln(m)$ leads to an increase of entropy and further the improvement of electroactivity. This means that without

the strain effect, utilizing the high index facets is able to achieve the equivalent electroactivity with HEA.[39] On the other hand, applying strain to the lower index facets is another strategy.[23,27]

Meanwhile, directly applying the mixing arrangements to Equation (1) also results in the following expression.

$$W_{total} = W_e \times W_{ion} \times W_{mix} = \exp\left[m^{\left(-\frac{E_0}{k_B T}\right)}\right] \quad (7)$$

Under this situation, when m >>1, we derive that $W_{total} \approx 1$, indicating that the total structural entropy S is approaching 0. This allows the reversible exchange of the atoms to achieve the high electroactivity, which explains the experimental phenomenon in previous works.[40]

Notably, all the elements show evident splitting for the surface energies dependence on the surface atom density in **Figure 6a-e**. The difference of the slopes for the two lines extrapolating the two groups of facets on each figure actually reflects the number of atoms contained in the outmost layer of the cleaved surface. With this correlation, our lattice models are classified into two types according to the number of surface layer atoms. The facets with less surface layer atom belong to the lower line with the larger slope, and the upper line with the smaller slope indicates the surface with more atoms. This evident classification supplies a straightforward method to predict the stability of the target high-index facets. For the d-band center variation with surface energy, the variation trends for different elements are hard to summarize (**Figure 6f-6j**). However, when applying the d-band center of an outmost single atom to correlate with the surface energy, from Fe to Pt, the d-band centers gradually diversifies into two groups, especially for Pd and Pt (**Figure 6k-6o**). The lower groups of facets of the Pd and Pt feature very narrow lattice widths and clear step-terrace surface structures (**Figure S6a-c)**. The upper groups of facets on Pd and Pt plots frequently present step-terrace-kink structures or with (110)

facets in either the steps or terraces (**Figure S6d-f)**. This means that the local lattice structures determine the chemical environment and reactivity of the surface atoms. This distinct splitting phenomenon disappears when it comes to Fe, Co, and Ni, which all have much smaller lattice parameters than Pd and Pt. Thus, such local surface structure induced electroactivity difference is only achieved when the lattice parameters are sufficiently large. The reported experimental reactivity differences for those facets within the same group should originate from the geometric factors.[41–44] In addition, since Fe, Co and Ni with different lattice structure types display similar behaviors in the relationship between surface atom density and d-band center, the splitting of the d-band center of high-index facets is independent of the specific phase structures.

2.7 Mapping the balance of surface activity, surface energy, and surface atom density

Additionally, to supply more references to the future experiment design for transition metal-based catalysts, the correlation among the surface energy, surface atom density and d-band center of the outmost surface atom is revealed. Interestingly, Fe shows the highest surface atom density correlates to the highest electroactivity, where the oxidation of Fe occurs and further lowers the catalysis efficiency (**Figure 7a**). Within the limited region of the surface atom density between 0.04 and 0.05, the appropriated-band position is able to preserve regardless of the surface stability, which should be the ideal region for electrocatalyst synthesis. In contrast, Co shows a relative inert feature, where the d-band center only varies in a small range, which indicates a good modulator of Co for tuning the electroactivity of alloy catalysts (**Figure 7b**). Apparently, Ni demonstrates the evident optimal synthesis range between the surface atom density of 0.05 to 0.12, where both the stability and activity are achieved simultaneously (**Figure 7c**). For Pt, the high electroactivity is reached by the sacrifice of the stability, where both high and small surface atom density limits the electroactivity (**Figure 7d**). Pd delivers a relatively symmetry trend. The ultra-small surface atom density such as singe atom is not

electroactive while the electroactivity and stability are able to be modulated for surfaces with a high density of surface atoms (**Figure 7e**). For both reported catalyst Pt_3Ni and Pt_3Fe, we notice that most stable morphology does not represent the highest electroactivity. The intermediate surface atom density is able to activate the intrinsic electroactivity for modulation (**Figure 7f-g**). For the ternary alloy PtNiCo, we notice that the intrinsic electroactivity has been dominated by Ni, where the highly electroactive catalyst with superior stability is realized (**Figure 7h**). Most importantly, we notice the evident volcano plot of HEA alloys by considering three individual factors, which solves the dilemma between stability, electroactivity and surface atom density (**Figure 7i**).[39] This supports the great potential for future electrocatalysis applications, which offers new opportunities for electrocatalyst design and development.

2.8 Adsorption energies mapping of the high-index facets

In order to have a comprehensive understanding of the electroactivity of the various facets of the elements, we choose the oxygen reduction reaction (ORR) process on Pd facets as the representative models, which is also easy to compare with reported works. The adsorption of O_2, *OOH and *OH have been considered since they are the key intermediates for ORR and oxygen evolution reaction (OER). **Figure 8a-c** present the facet formation energies, surface atom density and d-band center values of the bare Pt facet surfaces. We noticed the agglomeration of the facet energies and d-band center in high index-surfaces. The more evident fluctuations of the low index facets indicate their potential in the modulation of surface electroactivity. With the adsorbates, the adsorption energies show the reverse trends to that of the facet energies (**Figure 8d-f**). The low-index facets with smaller facet formation energies generally have higher adsorption energies for O_2, *OOH and *OH. Meanwhile, we notice that the adsorbates induced stability is applicable for all the facets. To further demonstrate the relations between the facet stability and adsorption ability, we propose the stabilization energy concept to indicates the stability change induced by the adsorbates to the surface. The majority

of the Pt facets feature positive O_2 stabilization energies while (531) surface is the only facet that becomes more stable after O_2 adsorption. These results indicate the important strain and perturbation induced by the reactants on the surface during electrocatalysis (**Figure 8g**). Meanwhile, as the key intermediates of rate-determining step (RDS), the adsorption of *OOH and *OH substantially stabilized the surfaces. The adsorptions of *OOH show slightly lower stabilization energies. These results represent the favorable trend of *OOH and *OH formation, which explains the holistically remarkable ORR reaction of Pt as a well-established consensus (**Figure 8h-i**).

In particular, we notice that Pt (110) has the much preferable energy trend for the formation of *OOH or *OH from O_2 adsorption, leading to an intrinsically superior activity of ORR than the (100) and (111) facets. This is also consistent with previous experimental studies of the ORR activity on Pt single-crystal surfaces, which follows the order: (110)>(111)>(100).[45,46] The high index facets of Pt are considered to have higher catalytic activity than the low-index facets due to stronger adsorption of the O-species.[47] More importantly, we find substantial consistency between our interpretations and the experimental cases. For example, the anisotropic {411}-faceted Pt catalyst has been reported to show evident catalytic activity enhancement to both OER and ORR [48]. In our calculation, compared to other facets, Pt (411) has O_2 stabilization energy close to zero, which is lower than most of the other facets. Hence, the initial adsorption of O_2 for ORR and the final removal of formed O_2 for OER are guaranteed. The OOH and OH stabilization energies for Pt (411) are also at a moderate level, which leads to facile reaction barriers of RDS in both OER and ORR. Moreover, previous studies also pointed out the high ORR activity high-index facets of Pt (211)[49], Pt (221)[50], and Pt (331)[50], which are in good agreement with the strong O_2 stabilization. In the meantime, the OOH and OH stabilizations on these facets are also firm enough to promote the ORR. Therefore, our work has demonstrated useful guidance for the experimental synthesis to predict and compare the

electrocatalyst performances, supplying constructive references for the catalyst design and modulations.

2.9 Perspectives and Outlooks

The introduction of other transition metals to the catalyst is another important optimization strategy to achieve higher catalytic activity and longer durability with a lower expense. The electroactivity of an alloy system with multi-element is generally affected by multiple factors simultaneously, which are classified into three fundamental effects: the ensemble effect, ligand effect, and strain effect [23]. The ensemble effect is raised by the formation of active pairs of atoms or ensembles on the surface, serving as the active sites. The ligand effect originates from the difference in electronic properties between the metals and results in electron transfers and perturbation of the electronic structure. The strain effect in alloy modulates the electronic structure modulation *via* the changes in the atomic arrangement, which is similar to the strain effect in the monometallic system. These three fundamental effects generally simultaneously present and co-impact the catalytic activity. However, considering their effective range in dimension, only the strain effect can impact the surface reactivity over the whole structure, especially when the material consists of a few atomic layers or a certain thickness of the shell.[23] For these structures (e.g. core-shell structure), the strain effect predominantly controls the modified electronic activity while the contributions of ensemble and ligand effects are very limited. More importantly, the analysis of alloy effect generally decouples the three fundamental effects based on the investigations through the control variable manner. Consequently, our models and discussions will be also valid for systems that are under the simultaneous impact of the ensemble, ligand, and strain effects. Although our work mainly focuses on the monometallic systems, we will further extend such exploration strategy to the bimetallic systems and even more complicated material systems. Moreover, our results and discussions about high-index facets and high-entropy alloys (HEAs) in previous sections are

also of significance for future research on electroactivity improvement of multi-element material systems.

3. Conclusion

During the investigation of the strain effect in late TM metals, the irregular electronic structure variations are confirmed, which reveals the zig-zag and volcano-like trends rather than the linear correlation in conventional theoretical models. For the low index surface, Co and Ni follow the traditional prediction while the Fe and Pd present completely different trends. The structural variations verify that the changes in interlayer bondlength and bonding conditions are the major contributions to the d-band center. The opposite impact on spin polarization by strain is also discovered. For the high-index facets, the surface atom density has been identified to be a universal descriptor for the stability and surface reactivity regardless of the specific elements and configurations. We have successfully confirmed the electroactivity of reported TM alloy catalysts and screen out the HEA as a promising catalyst candidate, which displays the three-dimensional volcano plot regarding electroactivity, stability, and surface atom density. Thus, this work not only offers novel insights based on the well-accepted interpretation of strain effect but also supplies the innovative electrocatalyst design strategy based on the new descriptor. These results are of pivotal significance to the further development of novel efficient TM electrocatalysts based on the constructive guidance to the experimental synthesis.

Acknowledgements
The authors gratefully acknowledge the support of the Natural Science Foundation of China (Grant No.: NSFC 21771156), and the Early Career Scheme (ECS) fund (Grant No.: PolyU 253026/16P) from the Research Grant Council (RGC) in Hong Kong.

Received: ((will be filled in by the editorial staff))
Revised: ((will be filled in by the editorial staff))
Published online: ((will be filled in by the editorial staff))

References

[1]. Turner, J. A. Sustainable hydrogen production. *Science* **305**, 972 (2004).

[2]. Tahir, M. *et al.* Electrocatalytic oxygen evolution reaction for energy conversion and storage: A comprehensive review. *Nano Energy* **37**, 136–157 (2017).

[3]. Dunn, S. Hydrogen futures: Toward a sustainable energy system. *International Journal of Hydrogen Energy* **27**, 235–264 (2002).

[4]. Dresselhaus, M. S. & Thomas, I. L. Alternative energy technologies. *Nature* **414**, 332–337 (2001).

[5]. Gao, X. *et al.* Mo isolated single atoms on s, n-codoped carbon as efficient catalyst for hydrogen evolution reaction: A theoretical evaluation. *Applied Surface Science* **473**, 770–776 (2019).

[6]. Greeley, J. *et al.* Alloys of platinum and early transition metals as oxygen reduction electrocatalysts. *Nature Chemistry* **1**, 552–556 (2009).

[7]. Jin, H. *et al.* Heteroatom-doped transition metal electrocatalysts for hydrogen evolution reaction. *ACS Energy Letters* **4**, 805–810 (2019).

[8]. Khorshidi, A., Violet, J., Hashemi, J. & Peterson, A. A. How strain can break the scaling relations of catalysis. *Nature Catalysis* **1**, 263–268 (2018).

[9]. Nørskov, J. K. *et al.* Origin of the overpotential for oxygen reduction at a fuel-cell cathode. *The Journal of Physical Chemistry B* **108**, 17886–17892 (2004).

[10]. Bu, L. *et al.* Biaxially strained PtPb/Pt core/shell nanoplate boosts oxygen reduction catalysis. *Science* **354**, 1410 (2016).

[11]. Chen, L. *et al.* Phase conversion of Pt_3Ni_2/C from disordered alloy to ordered intermetallic with strained lattice for oxygen reduction reaction. *Electrochimica Acta* **283**, 1253–1260 (2018).

[12]. Feng, Y. *et al.* An unconventional role of ligand in continuously tuning of metal–metal interfacial strain. *Journal of the American Chemical Society* **134**, 2004–2007 (2012).

[13]. Francis, M. F. & Curtin, W. A. Mechanical stress combined with alloying may allow continuous control over reactivity: Strain effects on co dissociation and subsequent methanation catalysis over Ni(211), Ni3Fe(211), and NiFe(112). *The Journal of Physical Chemistry C* **121**, 6113–6119 (2017).

[14]. Laurent, G., Martín, F. & Busnengo, H. F. Theoretical study of hydrogen dissociative adsorption on strained pseudomorphic monolayers of Cu and Pd deposited onto a Ru(0001) substrate. *Physical Chemistry Chemical Physics* **11**, 7303–7311 (2009).

[15]. Liu, F., Wu, C., Yang, G. & Yang, S. CO oxidation over strained pt(100) surface: A DFT study. *The Journal of Physical Chemistry C* **119**, 15500–15505 (2015).

[16]. Liu, M., Xin, H. & Wu, Q. Unusual strain effect of a Pt-based l10 face-centered tetragonal core in core/shell nanoparticles for the oxygen reduction reaction. *Physical Chemistry Chemical Physics* **21**, 6477–6484 (2019).

[17]. Luo, M. & Guo, S. Strain-controlled electrocatalysis on multimetallic nanomaterials. *Nature Reviews Materials* **2**, 17059 (2017).

[18]. Mavrikakis, M., Hammer, B. & Nørskov, J. K. Effect of strain on the reactivity of metal surfaces. *Physical Review Letters* **81**, 2819–2822 (1998).

[19]. Mendoza-Cruz, R. *et al.* Orthorhombic distortion in au nanoparticles induced by high pressure. *CrystEngComm* **21**, 3451–3459 (2019).

[20]. Moseley, P. & Curtin, W. A. Computational design of strain in core–shell nanoparticles for optimizing catalytic activity. *Nano Letters* **15**, 4089–4095 (2015).

[21]. Sakong, S. & Groß, A. Dissociative adsorption of hydrogen on strained Cu surfaces. *Surface Science* **525**, 107–118 (2003).

[22]. Schnur, S. & Groß, A. Strain and coordination effects in the adsorption properties of early transition metals: A density-functional theory study. *Physical Review B* **81**, 033402 (2010).

[23]. Strasser, P. *et al.* Lattice-strain control of the activity in dealloyed core–shell fuel cell catalysts. *Nature Chemistry* **2**, 454–460 (2010).

[24]. Sun, Y. *et al.* Ambient-stable tetragonal phase in silver nanostructures. *Nature Communications* **3**, 971 (2012).

[25]. Zhang, S. *et al.* Tuning nanoparticle structure and surface strain for catalysis optimization. *Journal of the American Chemical Society* **136**, 7734–7739 (2014).

[26]. Yao, Y. *et al.* Modulating fcc and hcp ruthenium on the surface of palladium–copper alloy through tunable lattice mismatch. *Angewandte Chemie International Edition* **55**, 5501–5505 (2016).

[27]. Yang, R., Leisch, J., Strasser, P. & Toney, M. F. Structure of dealloyed $PtCu_3$ thin films and catalytic activity for oxygen reduction. *Chemistry of Materials* **22**, 4712–4720 (2010).

[28]. Chen, G. *et al.* Oxygen reduction kinetics on pt monolayer shell highly affected by the structure of bimetallic AuNi cores. *Chemistry of Materials* **28**, 5274–5281 (2016).

[29]. Cui, C., Gan, L., Heggen, M., Rudi, S. & Strasser, P. Compositional segregation in shaped pt alloy nanoparticles and their structural behaviour during electrocatalysis. *Nature Materials* **12**, 765–771 (2013).

[30]. Wang, L. *et al.* Tunable intrinsic strain in two-dimensional transition metal electrocatalysts. *Science* **363**, 870 (2019).

[31]. Hammer, B. & Nørskov, J. K. Theoretical surface science and catalysis—calculations and concepts. *Advances in catalysis* vol. 45 71–129 (Academic Press, 2000).

[32]. Wang, H. *et al.* Direct and continuous strain control of catalysts with tunable battery electrode materials. *Science* **354**, 1031 (2016).

[33]. Luo, M. & Guo, S. Strain-controlled electrocatalysis on multimetallic nanomaterials. *Nature Reviews Materials* **2**, 17059 (2017).

[34]. Zheng, X., Li, L., Li, J. & Wei, Z. Intrinsic effects of strain on low-index surfaces of platinum: Roles of the five 5d orbitals. *Physical Chemistry Chemical Physics* **21**, 3242–3249 (2019).

[35]. Hyman, M. P. & Medlin, J. W. Effects of electronic structure modifications on the adsorption of oxygen reduction reaction intermediates on model Pt(111)-alloy surfaces. *The Journal of Physical Chemistry C* **111**, 17052–17060 (2007).

[36]. Xin, H., Vojvodic, A., Voss, J., Nørskov, J. K. & Abild-Pedersen, F. Effects of d-band shape on the surface reactivity of transition-metal alloys. *Physical Review B* **89**, 115114 (2014).

[37]. KOLMOGOROV, A. Sulla determinazione empirica di una lgge di distribuzione. **4**, 83–91 (1933).

[38]. Smirnov, N. Table for estimating the goodness of fit of empirical distributions. *Ann. Math. Statist.* **19**, 279–281 (1948).

[39]. Yao. Y. et al. Carbothermal shock synthesis of high entropy alloy nanoparticles. *Science*, **359**, 1489-1494 (2018)

[40]. Cao. L. et. al. Differential Surface Elemental Distribution Leads to Significantly Enhanced Stability of PtNi-Based ORR Catalysts, *Matter*, **1**, 1567-1580 (2019)

[41]. Hoshi, N., Kawatani, S., Kudo, M. & Hori*, Y. Significant enhancement of the electrochemical reduction of CO_2 at the kink sites on Pt(S)-n(110)×(100) and Pt(S)-n(100)×(110). *Journal of Electroanalytical Chemistry* **467**, 67–73 (1999).

[42]. Hoshi, N., Sato, E. & Hori, Y. Electrochemical reduction of carbon dioxide on kinked stepped surfaces of platinum inside the stereographic triangle. *Journal of Electroanalytical Chemistry* **540**, 105–110 (2003).

[43]. Hoshi, N. & Hori, Y. Electrochemical reduction of carbon dioxide at a series of platinum single crystal electrodes. *Electrochimica Acta* **45**, 4263–4270 (2000).

[44]. Hoshi, N., Suzuki, T. & Hori, Y. Catalytic activity of CO_2 reduction on Pt single-crystal electrodes: Pt(S)-n(111)×(111), Pt(S)-n(111)×(100), and Pt(S)-n(100)×(111). *The Journal of Physical Chemistry B* **101**, 8520–8524 (1997).

[45]. Marković, N. M. & Ross, P. N. Surface science studies of model fuel cell electrocatalysts. *Surface Science Reports* **45**, 117–229 (2002).

[46]. Wu, J. & Yang, H. Platinum-based oxygen reduction electrocatalysts. *Accounts of Chemical Research* **46**, 1848–1857 (2013).

[47]. Tian, N., Zhou, Z.-Y. & Sun, S.-G. Platinum metal catalysts of high-index surfaces: From single-crystal planes to electrochemically shape-controlled nanoparticles. *The Journal of Physical Chemistry C* **112**, 19801–19817 (2008).

[48]. Song, K. *et al.* Anisotropic surface modulation of Pt catalysts for highly reversible Li–O_2 batteries: High index facet as a critical descriptor. *ACS Catalysis* **8**, 9006–9015 (2018).

[49]. Ye, W. *et al.* Enhanced O_2 reduction on atomically thin Pt-based nanoshells by integrating surface facet, interfacial electronic, and substrate stabilization effects. *Nano Research* **11**, 3313–3326 (2018).

[50]. Kuzume, A., Herrero, E. & Feliu, J. M. Oxygen reduction on stepped platinum surfaces in acidic media. *Journal of Electroanalytical Chemistry* **599**, 333–343 (2007).

Figure 1

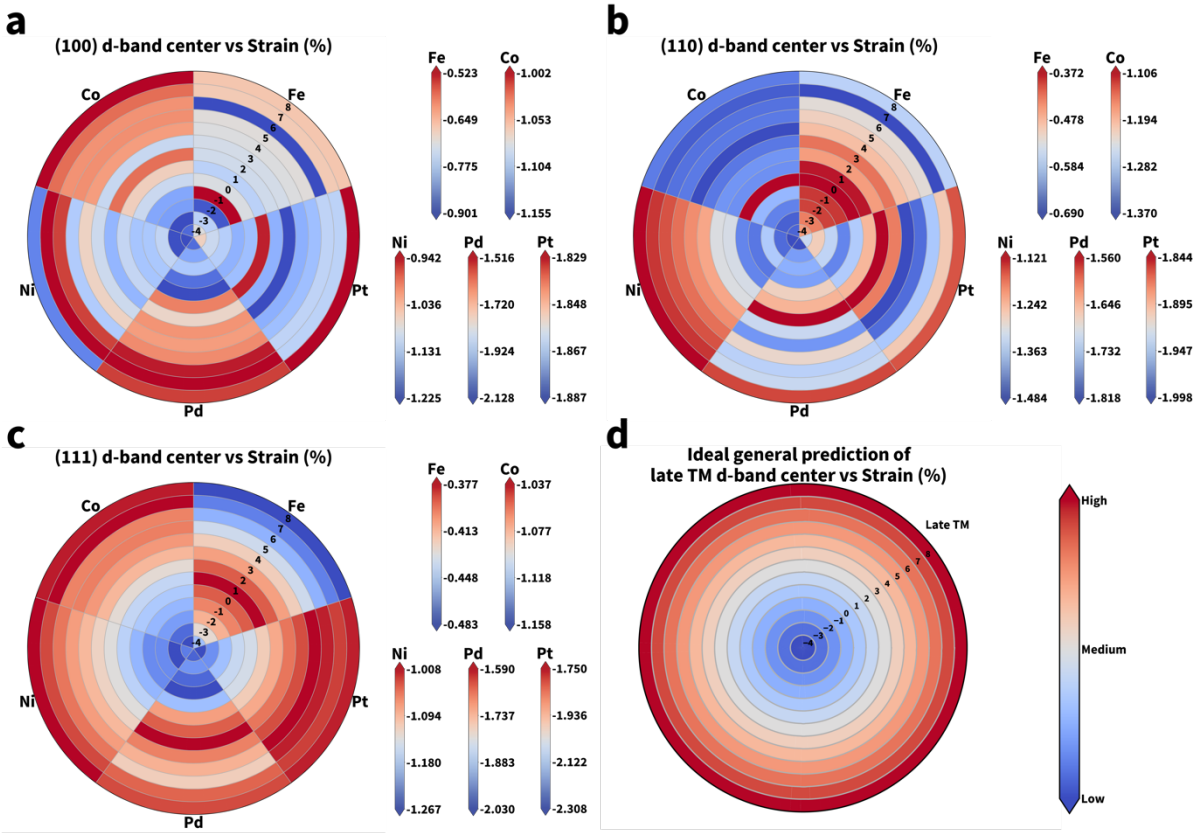

Figure 1. (a)-(c): The heatmap for comparison of strain effect on d-band center depth variations for the three low-index surfaces (a) (100), (b) (110), and (c) (111) of Fe, Co, Ni, Pd, and Pt. Each circle represents a strain level, and the colormap is assigned to each series individually to indicate the variation trend of the d-band center of each element and facet independently. The detailed d-band center levels of each facet and the mapping to colors are presented in the scale bars alongside. The scale bars are individual for each element. The d-band center trends for a facet under the varying strain are recognized with the change of color. The d-band center shifts from deeper to closer to Fermi level with color changing from blue to red. **(d)**: The ideal general prediction of late transition metal d-band center variation under strain is illustrated.

Figure 2.

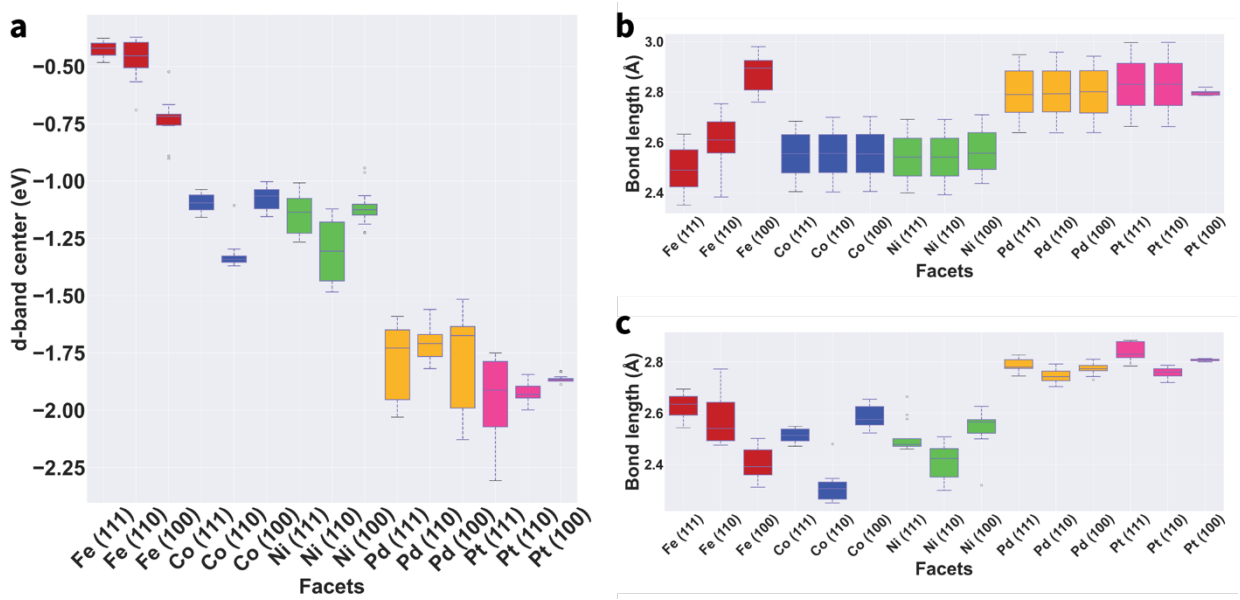

Figure 2. (a) The boxplot of the d-band centers for all elements and facet. **(b)** The boxplot for the average surface bond lengths for all elements and facets. It is noted that for Fe (100), at strain level larger than 5%, the central atom is isolated in the layer and its bondings are all with the subsurface layer, and hence the data for these levels are absent. **(c)** The boxplot for the average bondlengths between the surface central atoms and neighboring subsurface atoms, indicating the vertical distance between the two layers.

Figure 3.

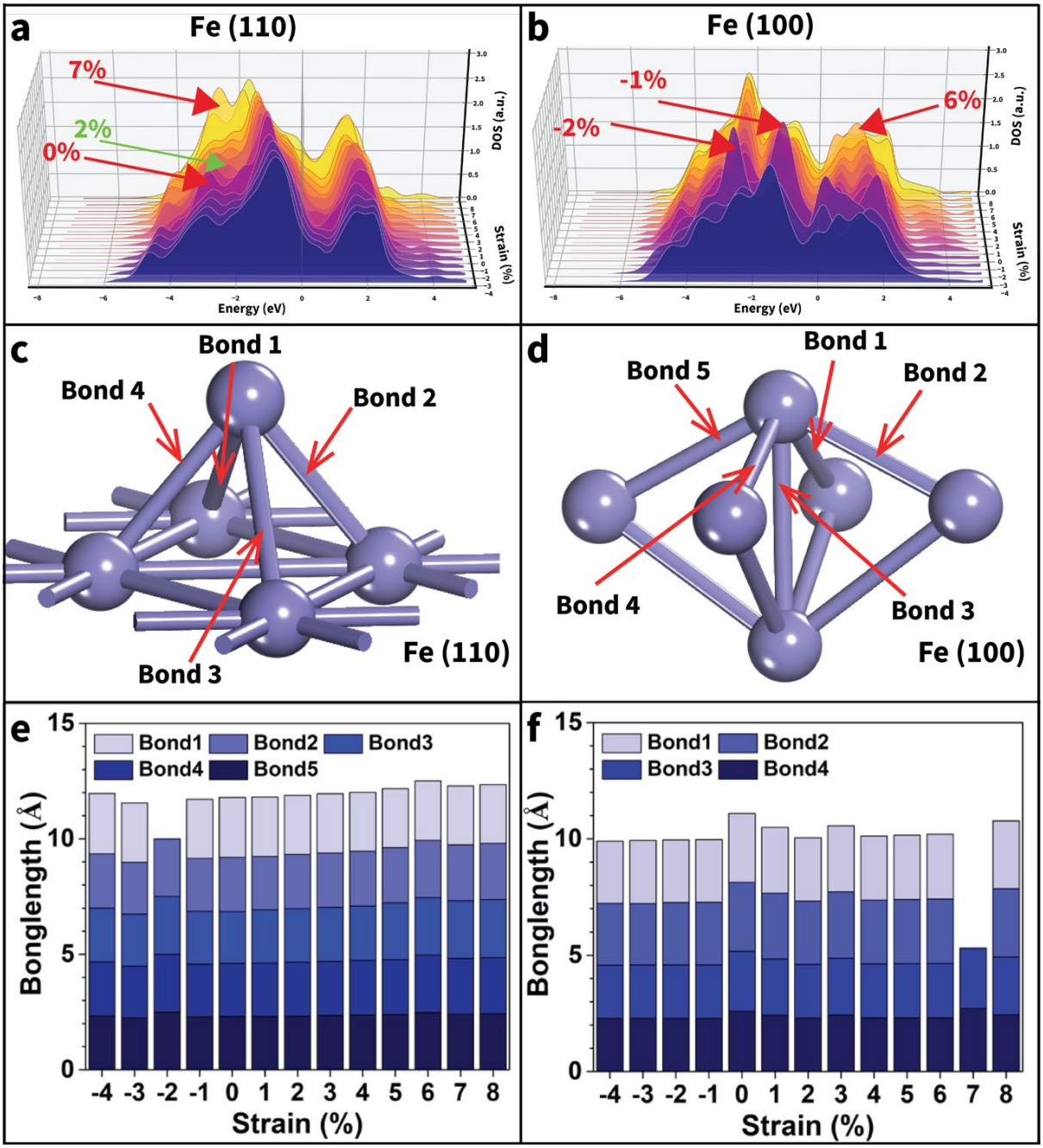

Figure 3. (a) The d-band DOS of Fe (110) surfaces under varying strain after geometry optimization. (b) The d-band DOS of Fe (100) surfaces under varying strain after geometry optimization. (c) Schematic illustration of the interlayer bonding scheme of Fe (110). (d) Schematic illustration of the interlayer bonding scheme of Fe (100). (e) The summarized bondlength of the Fe (110). (f) The summarized bondlength of Fe (100).

Figure 4.

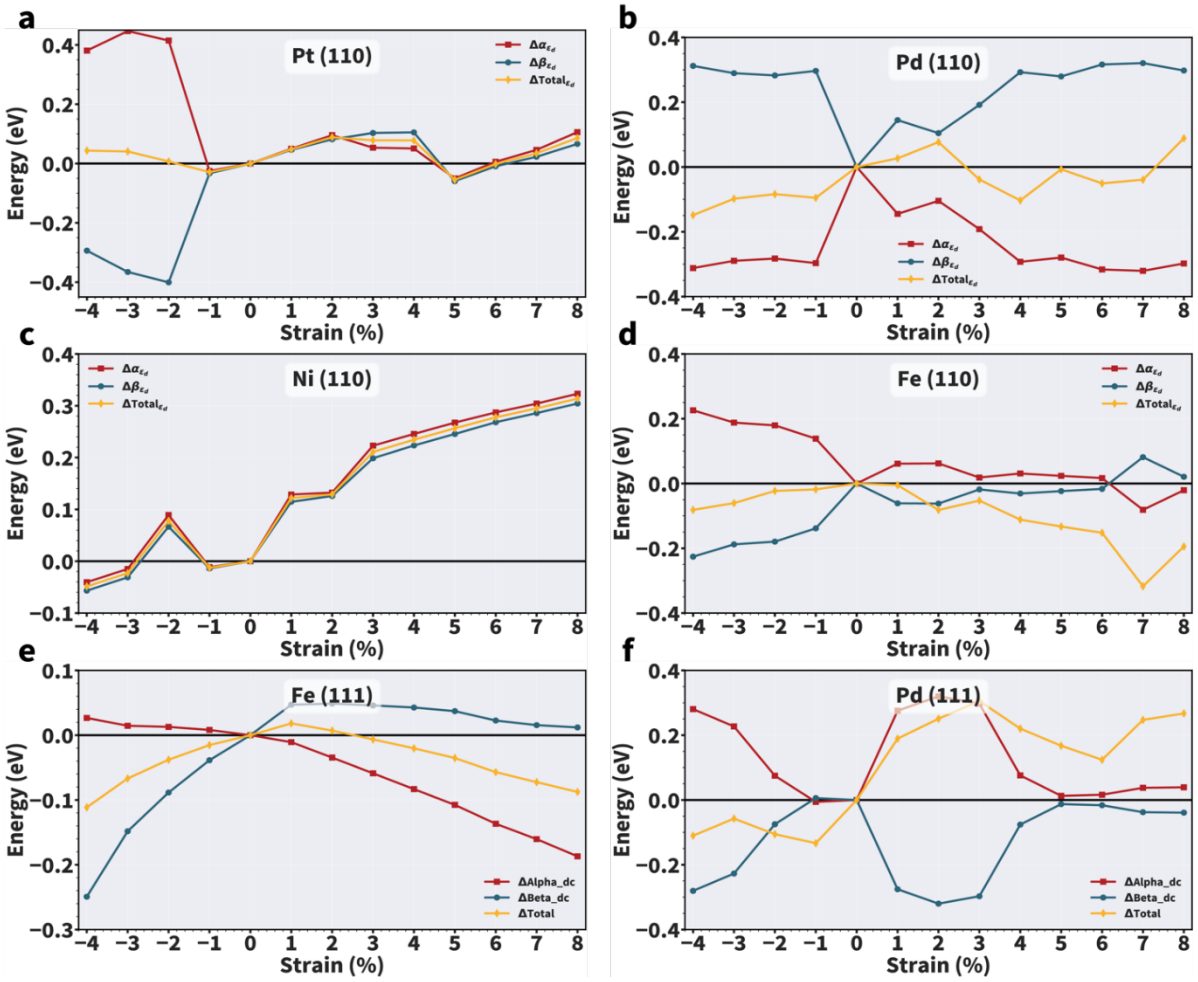

Figure 4. The spin-split view of d-band center shifts with strain of (a) Pt (110) , (b) Pd (110), (c) Ni (110), (d) Fe (110), (e) Fe (111), (f) Pd (111). The reference points are set as the d-band center values at zero applied strain for each facet. The positive value indicates the d-band center shifts upward compared to the non-strained state, whereas the negative value indicates the d-band center shifts downward compared to the non-strained state.

Figure 5.

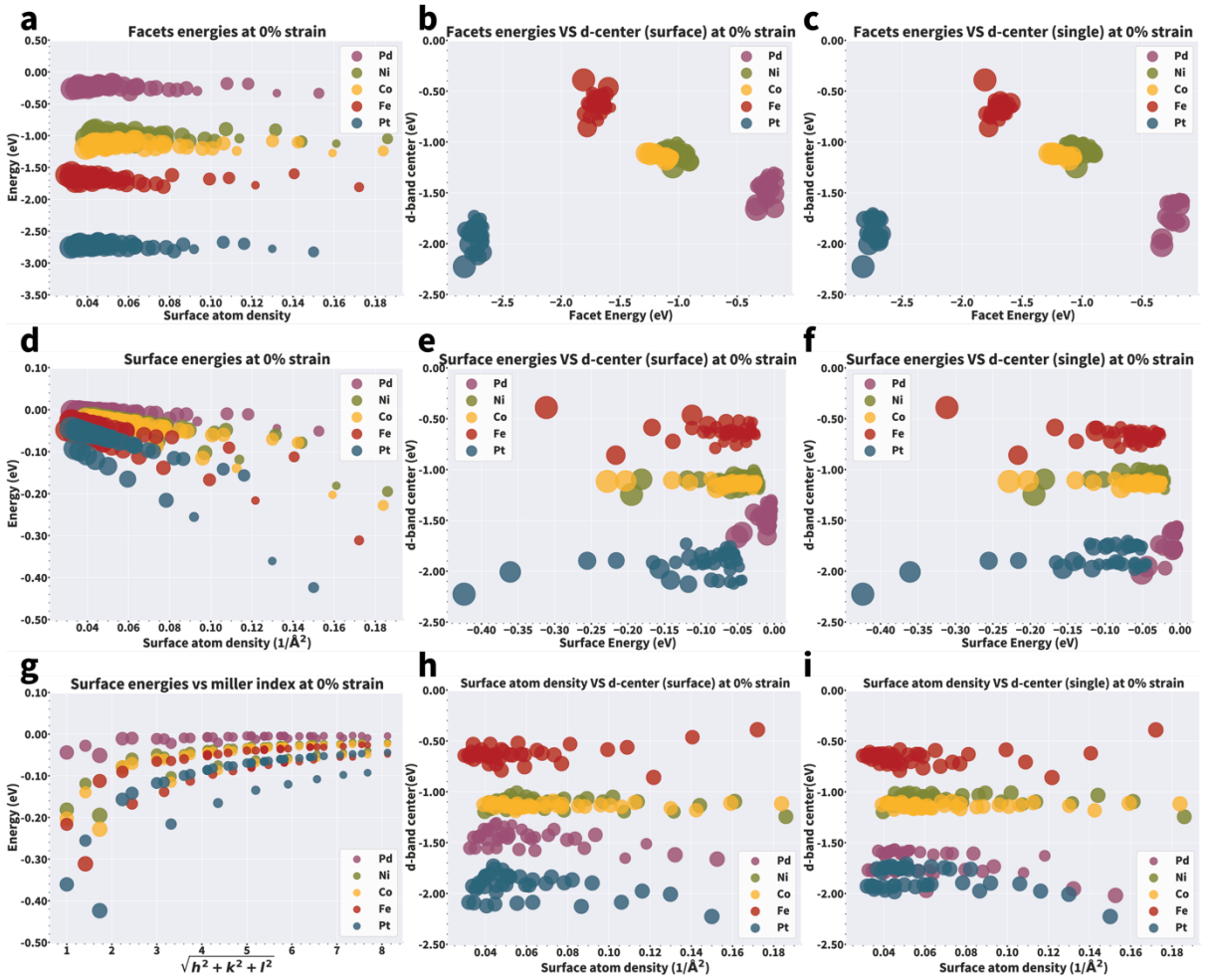

Figure 5. Correlation of facet energies, surface energies, d-band centers, surface atom density and miller indexes for the five late-transition metals. (**a**) Facet formation energies of Fe, Co, Ni, Pd and Pt facets against surface atom density. The scatter point sizes are scaled with the $\sqrt{h^2+k^2+l^2}$ of the facets, indicating the miller index. (**b**) The surface d-band centers for the five elements' facets plotted with the facet formation energies. The scatter point sizes are scaled with the surface atom densities. (**c**) The d-band centers for the atoms on the top of the surface, step edges or kink sites, plotted against the facet formation energies. The scatter point sizes are scaled with the surface atom densities. (**d**) Surface energies of the five elements' facets plotted against the surface atom density. The scatter point sizes are scaled with the $\sqrt{h^2+k^2+l^2}$ of the facets, indicating the miller index. (**e**) The surface d-band centers for the five elements' facets plotted with the surface energies. The scatter point sizes are scaled with the surface atom densities. (**f**) The d-band centers for the atoms on the top of the surface, step edges or kink sites, plotted against the surface energies. The scatter point sizes are scaled with the surface atom densities. (**g**) The surface energies plotted against the $\sqrt{h^2+k^2+l^2}$ of the facets, to demonstrate the energy evolution with the increase of miller-index. The scatter point sizes are scaled with the surface atom densities. (**h**) The surface d-band centers for the five elements' facets plotted with the surface atom density. The scatter point sizes are scaled with the surface atom densities. (**i**) The d-band centers for the atoms on the top of the surface, step edges or kink sites, plotted against the surface energies. The scatter point sizes are scaled with the surface atom densities.

Figure 6.

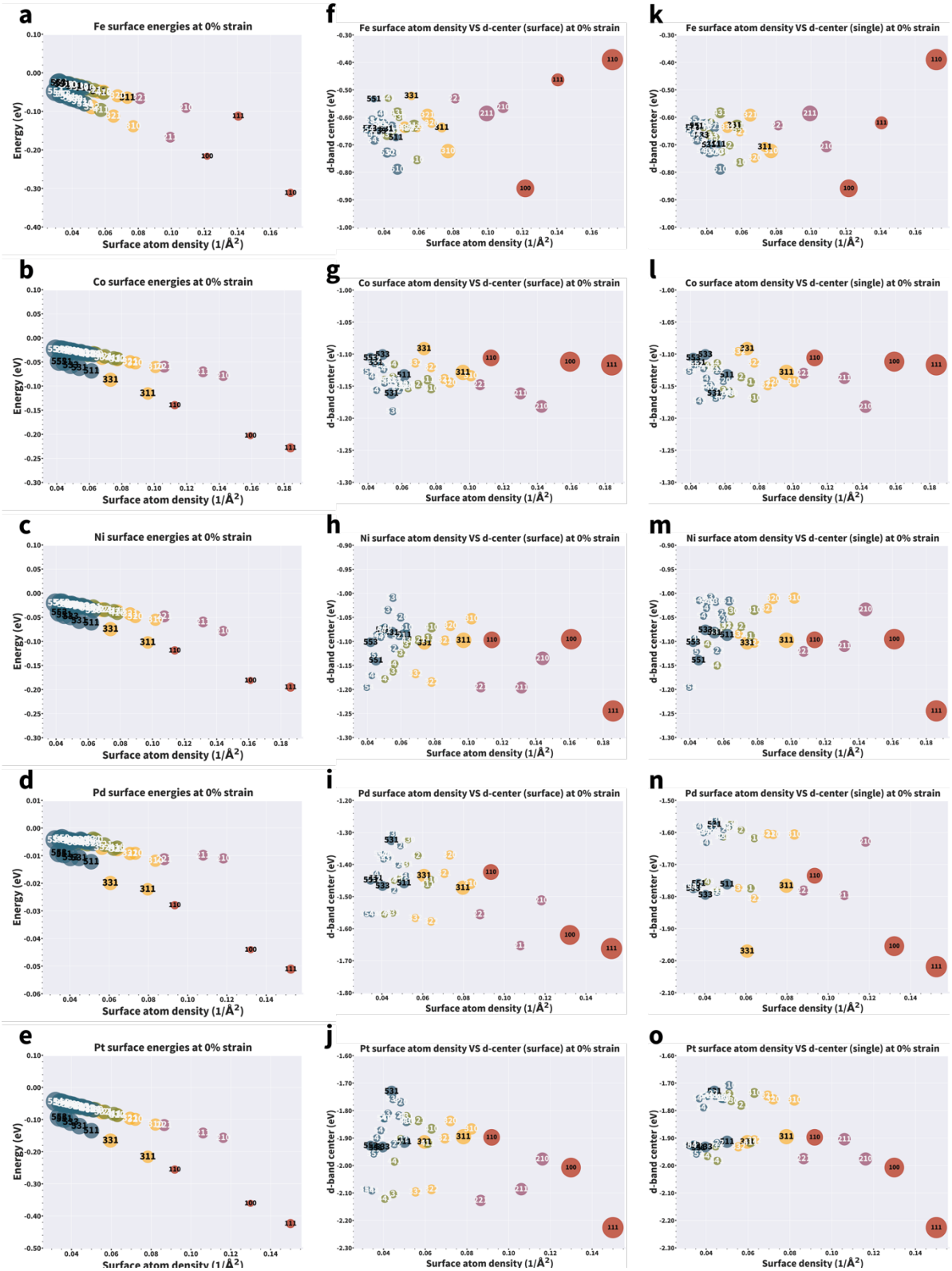

Figure 6. Element-wise plots of surface energies, surface atom densities and d-band centers for the whole layer of the atom on the ledge or kink. The surface energy dependence on the surface atom density for **(a)** Fe, **(b)** Co, **(c)** Ni, **(d)** Pd, **(e)** Pt. The d-band center (surface) dependence on the surface atom density for **(f)** Fe, **(g)** Co, **(h)** Ni, **(i)** Pd, **(j)** Pt. The d-band center (single) dependence on the surface atom density for **(k)** Fe, **(l)** Co, **(m)** Ni, **(n)** Pd, **(o)** Pt.

Figure 7.

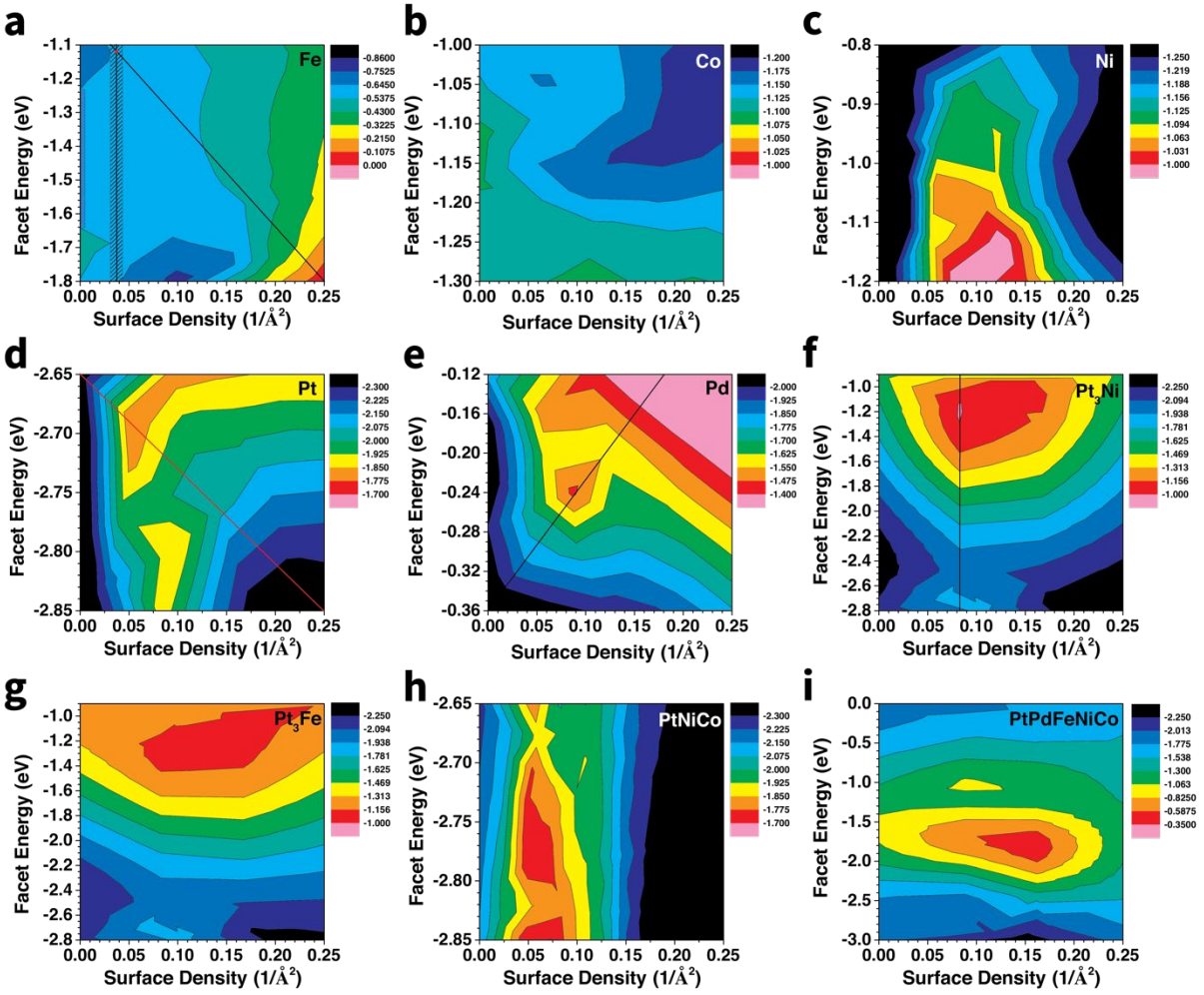

Figure 7. The contour fill plots by considering the surface energy, the electroactivity and the surface atom density for different materials. (a) Fe, (b) Co, (c) Ni, (d) Pt, (e) Pd, (f) Pt_3Ni, (g) Pt_3Fe, (h) PtNiCo, (i) PtPdFeNiCo HEA. The scale bars represent the d-band center.

Figure 8.

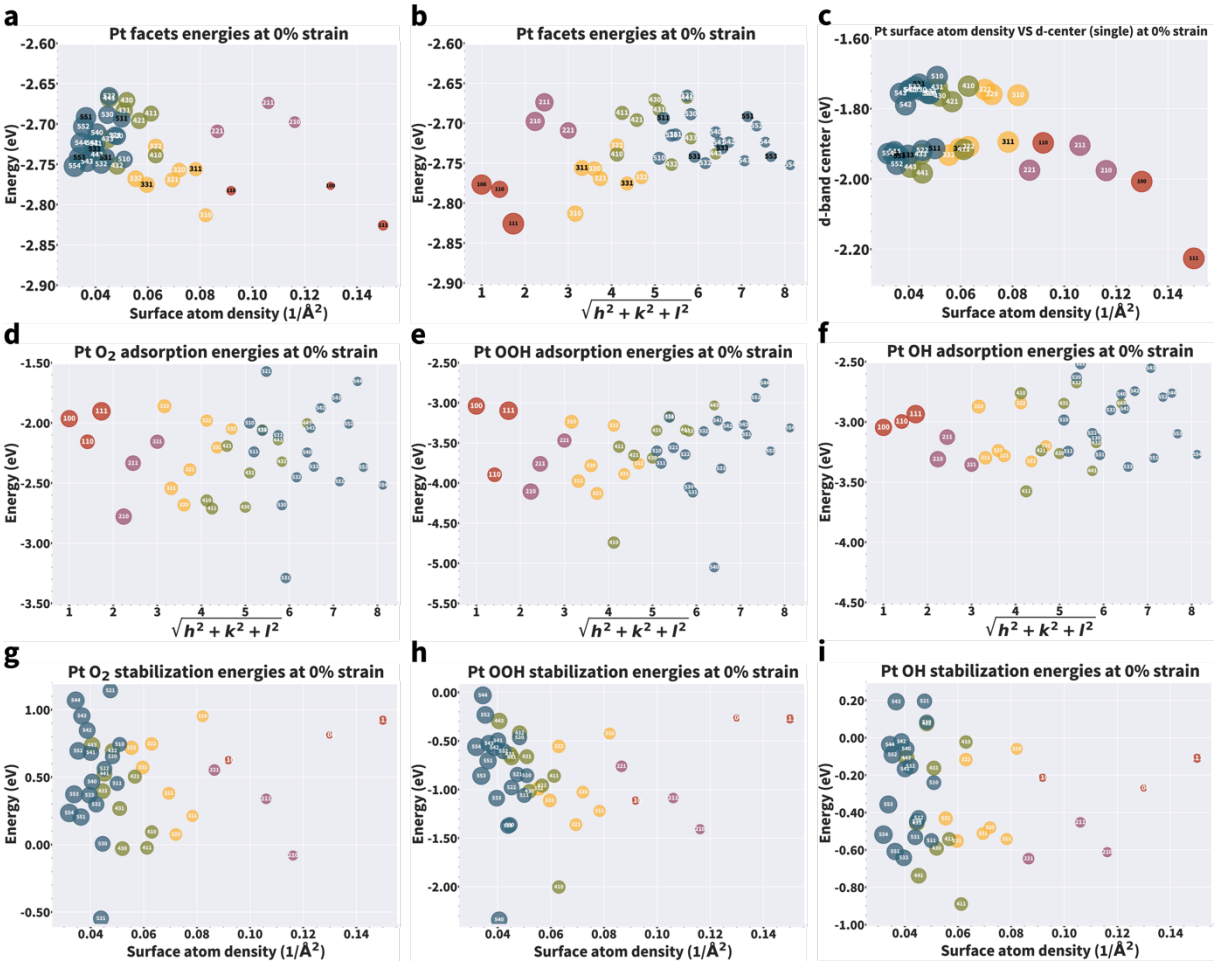

Figure 8. Adsorption energies of O_2, *OOH and *OH of Pt *from low to* high-index facets. (a-c) The facet formation energies, surface atom densities and d-band center of the surface atoms on the surface, step edges and kink sites for bare Pt surface at 0% strain. The scatter point sizes for (a-c) are scaled with the $\sqrt{h^2+k^2+l^2}$, surface atom densities and surface energies, respectively. (d-f) The O_2, *OOH and *OH adsorption energies plotted against the $\sqrt{h^2+k^2+l^2}$ of the facets of Pt. The scatter point sizes are scale with the surface atom densities. (g-i): The O_2, *OOH and *OH stabilization energies plotted against the surface atom densities of the facets of Pt. The scatter point sizes are scale with the $\sqrt{h^2+k^2+l^2}$.

The simplified strain effect in electroactivity has been extended based on our theoretical calculations for typical transition metals. By probing the irregular electronic structure with consideration of facet, an insightful understanding of typical strain effect on modulation of electroactivity in transition metal catalysts. This work supplies pivotal theoretical reference for future catalyst design.

Keyword: Strain Effect

T. W., M. S. and B. H*

Probing the irregular lattice strain-induced electronic structure variations on late transition metals for boosting the electrocatalyst activity